J Solid State Electrochem (2012) 16:1551–1559
DOI 10.1007/s10008-011-1558-6

ORIGINAL PAPER

Comparison of different soft chemical routes synthesis of submicro-$LiMn_2O_4$ and their influence on its electrochemical properties

Yongli Cui · Wenjing Bao · Zheng Yuan · Quanchao Zhuang · Zhi Sun

Received: 17 June 2011 / Revised: 9 September 2011 / Accepted: 20 September 2011 / Published online: 5 October 2011

Abstract A comparative study of submicro-crystalline spinel $LiMn_2O_4$ powders prepared by two different soft chemical routes such as hydrothermal and sol–gel methods is made. The dependence of the physicochemical properties of the spinel $LiMn_2O_4$ powder has been extensively investigated by using X-ray diffraction, Fourier transform infrared spectroscopy, scanning electron microscope, cyclic voltammogram, charge–discharge test, and electrochemical impedance spectroscopy (EIS). The results show that the electrochemical performances of spinel $LiMn_2O_4$ depend strongly upon the synthesis method. The $LiMn_2O_4$ powder prepared by hydrothermal route has higher specific capacity and better cycling performance than the one synthesized from sol–gel method. The former has the max discharge capacity of 114.36 and 99.78 mAh g^{-1} at the 100th cycle, while the latter has the max discharge capacity of 98.67 and 60.25 mAh g^{-1} at the 100th cycle. The selected equivalent circuit can fit well the EIS results of synthesized $LiMn_2O_4$. For spinel $LiMn_2O_4$ from sol–gel method and hydrothermal route in the first charge process R_{SEI} remain almost invariable, R_e and R_{ct} first decreasing and then increasing with the increase of polarization potential.

Keywords Lithium ion batteries · Spinel $LiMn_2O_4$ · Sol–gel · Hydrothermal · Electrochemical properties · Electrochemical impedance spectroscopy

Y. Cui (✉) · W. Bao · Z. Yuan · Q. Zhuang (✉) · Z. Sun
School of Materials Science and Engineering,
China University of Mining and Technology,
Xuzhou 221116, China
e-mail: lilyshuoxu@163.com
e-mail: zhuangquanchao@126.com

Introduction

At present, lithium-ion batteries, owing to the best energy-to-weight ratios, no memory effect, and a slow loss of charge when not in use, have been used in a wide variety of portable electric devices [1, 2]. It is well-known that the capacity of lithium-ion batteries is usually limited by cathode, and among the different materials ($LiCoO_2$, $LiNiO_2$, $LiFePO_4$, $LiMn_2O_4$, and so on) that have been considered as lithium intercalating cathodes, lithium manganese oxide ($LiMn_2O_4$) is one of the most promising cathode materials for its abundance of manganese, cost-effective, low toxicity and high energy density [3–5]. At room temperature, $LiMn_2O_4$ shows a cubic spinel-type structure, Fd3m space group, which structure can be described as ideally consisting of a cubic close-packed arrangement of oxygen ions at 32e sites, the Li^+ ions occupy the tetrahedral 8a sites and the Mn^{3+} and Mn^{4+} ions occupy the octahedral 16d sites. In the cubic phase, lithium extraction/insertion from/into the tetrahedral 8a sites occurs at 4 V, which is associated with the $Mn^{3+} \rightleftarrows Mn^{4+}$ oxidation and reduction process [6–9].

Conventionally, lithium manganese oxide powders are synthesized by a solid-state reaction of lithium and manganese salts [10, 11], which have inhomogeneity, irregular morphology, larger particle size with broad particle size distribution, poor control of stoichiometry, and longer period of calcinations followed by grinding. Recently, some chemical methods have been reported with several advantages such as good homogeneity, low calcination temperatures with uniform sub-micron size particles, which is an important factor in achieving high battery performance [12–14]. Considering the importance and significance of synthesis method, two different soft chemical route synthesis methods for $LiMn_2O_4$ cathode material,

viz, hydrothermal method, known as a low-temperature method to prepare submicron-sized particles and sol–gel method, known for the homogenous distribution of product, have been chosen for the present study.

Experimental

Experimental methods

$LiMn_2O_4$ was prepared by sol–gel method. Stoichiometric amounts of reactants $C_6H_8O_7{\cdot}H_2O$ (AR, Chemical Reagent Co. Ltd, Shanghai, China), $C_4H_6MnO_4{\cdot}4H_2O$ (AR, Sinopharm Chemical Reagent Co. Ltd, China), and Li_2CO_3 (AR, Sinopharm Chemical Reagent Co. Ltd, China) were dissolved in distilled water to form a mixed aqueous solution. Then, the solutions were added dropwise to a 6–7 pH of ammonium hydroxide (Xuzhou, 25–28% solution, China). The resultant solution continuous stirring at 80 °C until a transparent gel was obtained. Later, the prepared gel was heated to 120 °C for 12 h to remove water. The dry residue was further heat-treated at 350 °C for 2–3 h to cause a reaction. The black precursors were sintered at 750 °C for about 12 h in air at a heating rate of 3 °C min^{-1}. As prepared compound was found to be black in color and the $LiMn_2O_4$ powder as such was subjected to further studies.

In hydrothermal route, a solution consisting of MnO_2 (AR, Kermel Chemical Reagent Development Center, Tianjin, China) which before was already milled for 6 h at a 450 rpm rate in Planetary Ball Mill and $LiOH{\cdot}H_2O$ (AR, West Long Chemical Co., Ltd. Shantou, China) (molar ratio of Mn/Li=1:1) was added into the distilled water with vigorous stirring for 30 min. A black solution obtained was transferred into a 100-ml Teflon-lined stainless steel autoclave. The autoclave was sealed for 96 h at 180 °C, and then cooled naturally to room temperature. The formed precipitate was filtered and washed twice with double distilled water. The washed precipitate was further dried at 110 °C for 12 h and obtained the final $LiMn_2O_4$ product.

For the electrochemical properties of the products, the $LiMn_2O_4$ electrode used in this study were prepared by spreading a mixture comprising, by weight, 80% $LiMn_2O_4$, 3% acetylene black (Shanshan Co., Shanghai China), 7% mesocarbon microbeads, and 10% polyvinylidene fluoride (PVDF, Kynar FLEX 2801, Elf Atochem, USA) binder dissolved in *N*-methyl-2-pyrrolidone (Fluka Inc.) onto an aluminum foil current collector. The obtained electrode film was dried at 120 °C for 12 h under vacuum before to use. The electrolyte was 1 mol L^{-1} $LiPF_6$-EC/DEC/DMC (1:1:1, *v*/*v*/*v*, Guotaihuarong Co., Zhangjiagang, China).

Coin cells were assembled using lithium metal as the second electrode and were tested on the battery testing equipment (2XZ-2B, Neware Electronic Co. Ltd., Shenzhen, China). And the cyclic voltammogram (CV) measurements was measured at a sweep rate of 0.1 mVs^{-1} between 3.3 and 4.3 V. AC impedance measurements were performed over the frequency range of 10^5–10^{-2} Hz with an amplitude of 5 mV. The electrodes were kept for 1 h so that the system was stable before CV and AC impedance measurements.

Characterization

The phase identification of $LiMn_2O_4$ was carried out by powder X-ray diffraction (XRD) technique on a Rigaku D/Max-3B diffractometer using CuKα radiation. Diffraction data were collected by step scanning over an angular range of 15–75° with a step width of 0.02° at a scanning rate of 3° per minute. The vibrational spectra of $LiMn_2O_4$ were characterized by Fourier transform infrared spectroscopy (FTIR, Tensor-27, BRUKER) using a pellet containing a mixture of KBr and the response of active material in the region 400–1,200 cm^{-1}. The surface morphologies of synthesized samples were examined with a scanning electron microscopy (SEM, LEO 1530, Oxford Instrument).

Results and discussion

The structure and the morphology of spinel $LiMn_2O_4$

Figure 1 shows XRD pattern for the hydrothermal and sol–gel-derived materials, respectively. Spinel-type XRD pattern is observed for all the samples with characteristic (h kl) lines as indexed. From Fig. 1, XRD analysis showed a single phase of spinel $LiMn_2O_4$ exhibiting the Fd3m space with no impurity. It is very interesting to note that the (220) diffraction line that originated only from the tetrahedral Li-ion site in the spinel structure, is not observed in our materials, which means that manganese ions are not displaced into tetrahedral sites and only Li-ions with very

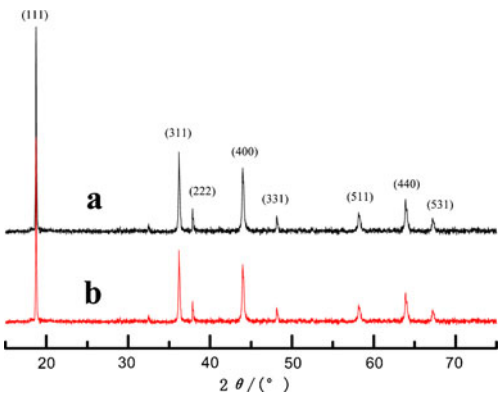

Fig. 1 XRD patterns of $LiMn_2O_4$ synthesized from hydrothermal and sol–gel methods (*a* sol–gel method, *b* hydrothermal route)

small scattering factor occupy the sites [12]. What is more, the sharper the intensities of diffraction peak, the better the crystallinity of the $LiMn_2O_4$ spinel phase was from both the hydrothermal route and sol–gel method.

FTIR spectrums of the synthesized $LiMn_2O_4$ spinel recorded at room temperature are shown in Fig. 2. Here, the FTIR spectrums are dominated by two strong absorption bands between 650 and 500 cm^{-1}, which are attributed to the asymmetric stretching modes of the MnO_6 group [15], i.e., the stretching band of O–Mn(IV)–O and Mn(III)–O. But the Li–O stretching has not been observed, that is the overlap of the Li–O and Mn–O vibration. Himmrich and Luta [16] reported that the vibrational modes of transition metal oxide spinels are attributed to all the atoms in the framework. Compared with that of the sol–gel synthesized $LiMn_2O_4$, the stretching band of the hydrothermal-derived $LiMn_2O_4$ has a blue shift to 618 cm^{-1} for the O–Mn(IV) bond and to 523 cm^{-1} for the Mn(III)–O bond, respectively. This implies that the $LiMn_2O_4$ prepared by hydrothermal has more stabile spinel structure than that of the sol–gel synthesized $LiMn_2O_4$. The Mn–O vibration peak becomes much sharper than that of the sol–gel synthesized $LiMn_2O_4$, which implies the appearance of a large ration of Mn^{3+}/Mn^{4+} [15] and more perfect lattice [17] for the hydrothermal route $LiMn_2O_4$. Therefore, the hydrothermal route $LiMn_2O_4$ has better electrochemical performance than that by sol–gel method.

Figure 3 shows SEM micrographs recorded for $LiMn_2O_4$ synthesized by hydrothermal and sol–gel methods individually. Both synthesized methods $LiMn_2O_4$ compounds have clearly definite octahedral shape, and their particles crystallized well with submicro-sizes. Particularly, $LiMn_2O_4$ compound synthesized by hydrothermal method (Fig. 3b) are found to contain homogenously ideal distributed octahedral grains with definite interparticle boundary. The low-temperature-aided hydrothermal synthesis is found to be advantageous in producing such a desirable morphology with submicro-crystalline particles,

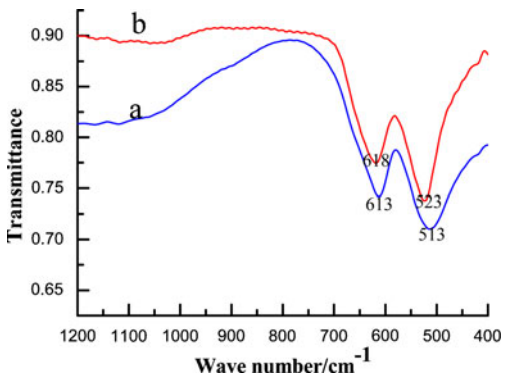

Fig. 2 FTIR spectrums of $LiMn_2O_4$ prepared by sol–gel and hydrothermal (*a* sol–gel method, *b* hydrothermal route)

which is the significance of hydrothermal method. So $LiMn_2O_4$ compounds synthesized using hydrothermal approach is expected to exhibit better electrochemical behavior. However, sol–gel method $LiMn_2O_4$ materials (Fig. 3a) are found to have some agglomerated particles with blur grain boundaries. The formation of irregular grain piles is believed to result from the high-temperature heat treatment (750 °C) deployed in sol–gel method.

The electrochemical performance of spinel $LiMn_2O_4$

Figure 4 demonstrates the cycling reversibility behavior of synthesized $LiMn_2O_4$ using two different synthesis methods at a scan rate of 0.1 mV s^{-1} in the potential ranging from 3.3 to 4.3 V. For $LiMn_2O_4$ cathodes, the CV consists of two anodic peaks and two cathodic peaks, corresponding to the two-step reversible de-intercalation and intercalation of lithium according to the following reactions [18–21]:

$$LiMn_2O_4 \rightleftarrows Li_{0.5}Mn_2O_4 + 0.5Li^+ + 0.5e^- \quad (1)$$

$$Li_{0.5}Mn_2O_4 \rightleftarrows \lambda - MnO_2 + 0.5Li^+ + 0.5e^- \quad (2)$$

The first pair of peaks (about 4.1 V/3.9 V) is attributed to the removal/addition of Li ion from/into a half the tetrahedral sites in which Li/Li^+ interaction occurs. The second redox pair (4.25 V/4.1 V) is attributed to the intercalation/de-intercalation of lithium into the other half of the tetrahedral sites, where Li^+ ions do not interact. It is well-known that these processes are accompanied by the reversible Mn^{3+}/Mn^{4+} redox reactions.

However, for $LiMn_2O_4$ prepared by hydrothermal route, the first pair redox peak and the second redox pair peak are not so enough sharp and completely separate as those of sol–gel methods. These mean the two-step process is not obvious, that is the two stages of insertion and extraction of lithium ions occur at the same time, indicating that the mechanism certainly changed.

Figure 5 shows the potential vs. discharge capacity of the Li/1M $LiPF_6$-EC/DEC/DMC electrolyte/$LiMn_2O_4$ cells with the cycle number (Fig. 6) at 0.1 °C rate (1 °C=148 mA/g). It is obvious that discharge curves of the samples have two voltage plateaus at approximately 4.0 and 4.1 V respectively, corresponding to the two stages of insertion and extraction of lithium, which mirror the two redox of CV. The capacity of $LiMn_2O_4$ obtained from both hydrothermal and sol–gel methods decreases slowly with the cycle number. Fading capacity of the spinel $LiMn_2O_4$ is due to Jahn–Teller distortion [22, 23], the dissolution of manganese into electrolyte [24–26], loss of crystalline during cycling [27], and electrolyte decomposition at high-potential regions [28–30]. The $LiMn_2O_4$ powders prepared by hydrothermal route

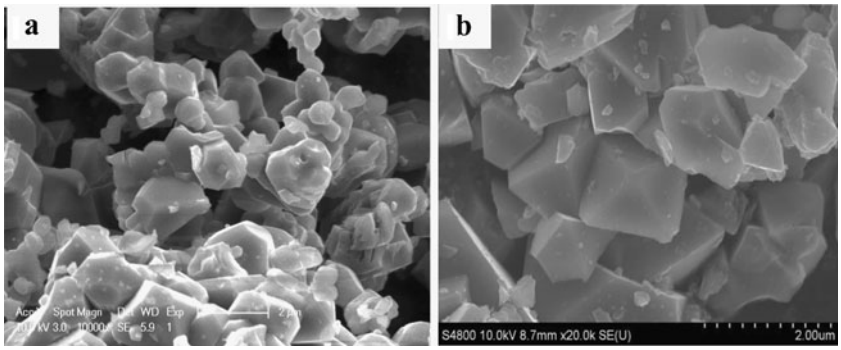

Fig. 3 SEM micrographs of $LiMn_2O_4$ prepared from **a** sol–gel method **b** hydrothermal route

shows initial discharge capacity 104.18 mAh g^{-1}, the max discharge capacity 114.36 mAh g^{-1}; after over 100 cycles, the capacity retention is still above 90%, indicating an excellent electrochemical performance. However, the initial specific discharge capacity of the spinel $LiMn_2O_4$ prepared by sol–gel is only close to 80.55 mAh g^{-1}, the max discharge capacity to 98.67 mAh g^{-1}; after over 100 cycles, its retention of capacity gets to 74.7%, indicating poor cycle performance.

It is inferred from the above results that the electrochemical performance of spinel $LiMn_2O_4$ depend strongly upon the synthesis method, that is $LiMn_2O_4$ powder prepared by hydrothermal route has higher specific capacity and better cycling performance than the one synthesized from sol–gel method. This further specified that the lithium inserted and the reversibility of lithium insertion/extraction reactions depend strongly upon the synthesis conditions [31] and even with the same chemical composition and crystal structure, small variations in physical properties of the cathode materials, such as surface morphology and size of the particle, influence the performance of the battery to a noticeable extent [32].

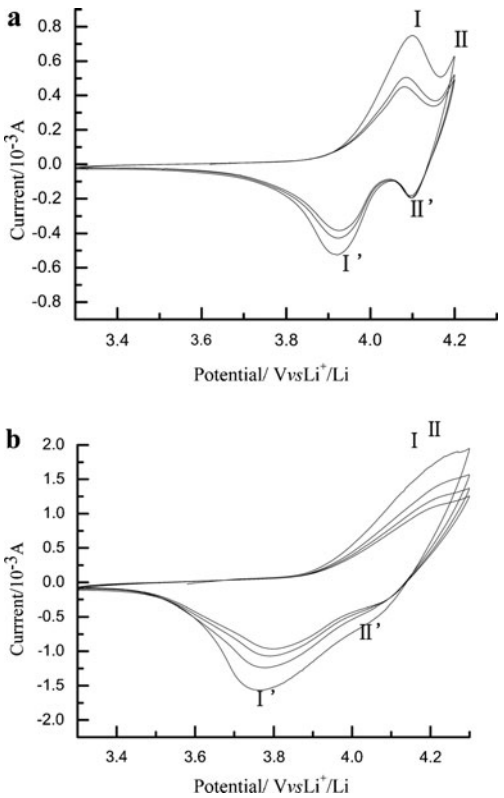

Fig. 4 Cyclic voltammogram of $LiMn_2O_4$ samples from sol–gel method and hydrothermal route at 0.1 mV s^{-1} scan rate (*a* sol–gel method, *b* hydrothermal route)

Electrochemical impedance spectroscopy of spinel $LiMn_2O_4$

To investigate the lithium-ion insertion mechanism at the electrode/electrolyte interface, EIS was conducted for the $LiMn_2O_4$ electrode during the first charge cycle in the 1 mol L^{-1} $LiPF_6$-EC/DEC/DMC electrolyte at room temperature. Nyquist plots of the synthesized $LiMn_2O_4$ cathodes in the potential region from 3.7 to 4.3 V during the first charge process are shown in Fig. 7. From Fig. 7, it can be seen that the $LiMn_2O_4$ prepared by different methods have similar EIS. Each Nyquist plot for $LiMn_2O_4$ cathodes below 3.85 V is composed of compressed semicircle in high-frequency region and a huge arc at medium-to-low frequencies. As the polarization potential increased, the high-frequency semicircle was gradually exaggerated, which obtained at room temperature was

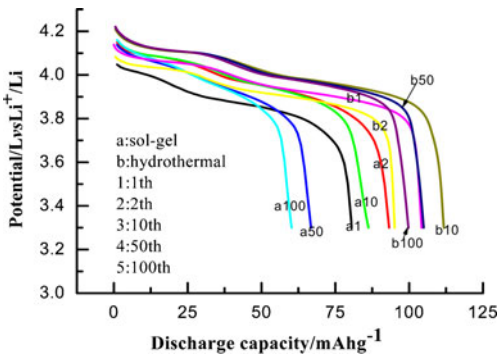

Fig. 5 Discharge curves of $LiMn_2O_4$ samples from hydrothermal route and sol–gel method

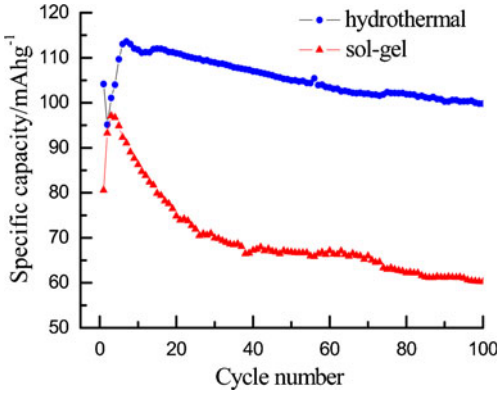

Fig. 6 Variation of discharge capacity with number of cycles for $LiMn_2O_4$ obtained from both hydrothermal route and sol–gel method

consisted of two semicircles actually [33], that is a high-frequency semicircle and a middle-to-high frequency semicircle (as marked in Fig. 7) and the middle-to-low frequency arc gradually formed another middle-frequency semicircle and a Warburg region followed by a steep sloping line at the low frequency. When at intermediate intercalation degrees, take 3.95 V for example, the Nyquist plot were consisted of four parts, qualitatively "three semicircles and one line," i.e., the high-frequency semicircle (abbreviated as HFS), the middle-to-high frequency semicircle (MHFS), the middle-frequency semicircle (MFS), and a steep sloping line in the low-frequency region (here called LFL in short). According to Gnanaraj's and Aurbach's opinions [34, 35], the HFS is related to lithium-ion migration through the SEI film covered on the spinel $LiMn_2O_4$, the MFS is attributed to charge transfer through the electrode/electrolyte interface, and LFL is assigned to solid-state diffusion of lithium ion in the $LiMn_2O_4$ matrix. In our previous studies [33], the MHFS was related to the electronic properties of the $LiMn_2O_4$ material.

Moreover, the delithiation potential and the impedance value are different in the EIS of $LiMn_2O_4$ cathodes prepared by two different synthesis methods. The medium frequency semicircle to charge-transfer reaction emerges in the potential region from 3.75 to 3.8 V for hydrothermally synthesized $LiMn_2O_4$ and in the 3.85–3.9 V range for $LiMn_2O_4$ by sol–gel method, which corresponds to the results of CV.

According to the experimental results above, an equivalent circuit, as shown in Fig. 8, is proposed to fit the impedance spectra of $LiMn_2O_4$ synthesized by hydrothermal method in the first charge process. In this equivalent circuit, R_s represents the ohmic resistance; R_{SEI} and R_{ct} are resistances of the SEI and the charge-transfer reaction; the capacitance of the SEI, the capacitance of the double layer are represented by the constant phase elements (CPE) Q_{SEI} and Q_{dl}, respectively; The low-frequency region, however, cannot be modeled properly by a finite Warburg element; we chose therefore to replace the finite diffusion by a CPE,

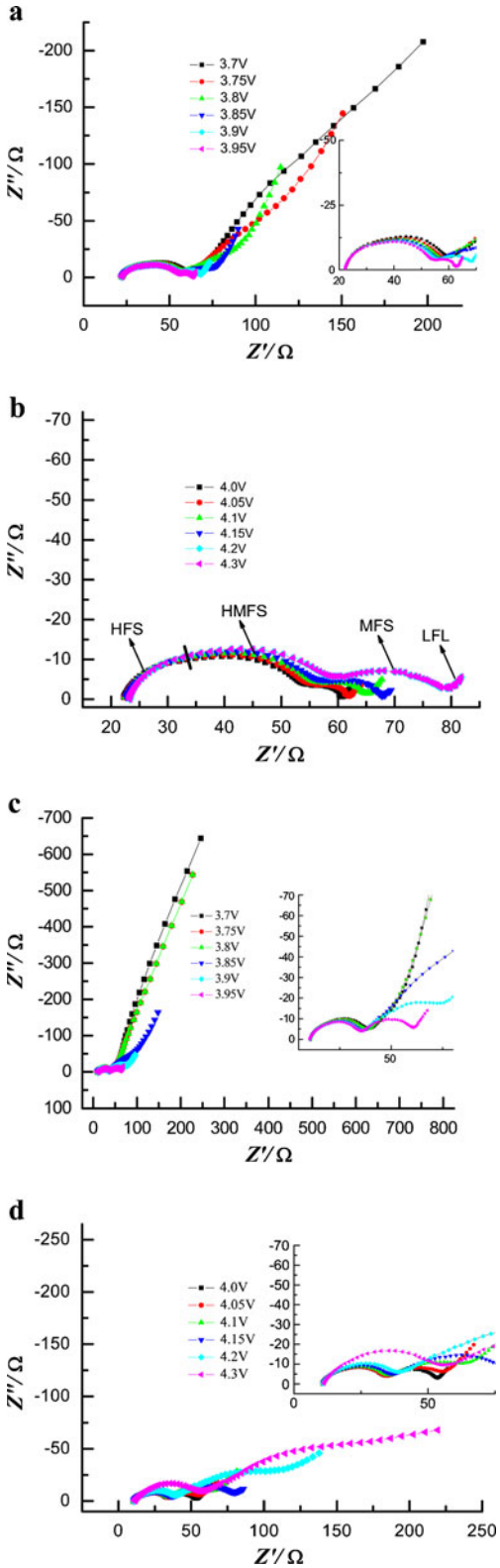

Fig. 7 EIS plots of spinel $LiMn_2O_4$ obtained from both hydrothermal and sol–gel method during the charge process (**a**, **b**, hydrothermal route; **c**, **d**, sol–gel method)

i.e., Q_D. The electronic resistance of the material and the associated capacitance used to characterize the electronic

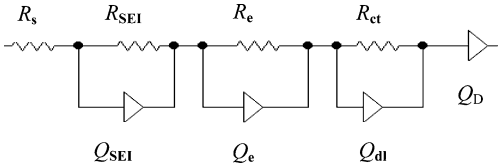

Fig. 8 Equivalent circuit proposed for analysis of the spinel $LiMn_2O_4$ electrode in the first charge process

properties of the material are represented by R_e and the constant phase elements Q_e. The expression for the admittance response of the CPE (Q) is

$$Y = Y_0\omega^n\cos\left(\frac{n\pi}{2}\right) + jY_0\omega^n\sin\left(\frac{n\pi}{2}\right), \quad (3)$$

where ω is the angular frequency, j is the imaginary unit. A CPE represents a resistor when n=0, a capacitor with capacitance of C when n=1, an inductor when n=−1, and a Warburg resistance when n=0.5.

At last the equivalent circuit was simulated by the software of Zview. Figure 9 shows the simulated impedance spectra compared with experimental EIS data of $LiMn_2O_4$ from hydrothermal route at 3.95 V in the charge process, and the values of parameters are listed in Table 1, the relative standard deviations for all parameters obtained from fitting the experimental impedance spectra, did not exceed 15%. It can be seen that the proposed model describes the experimental data satisfactorily.

Analysis of the equivalent circuit of EIS in initial charge process

Variations of resistances of the SEI and the charge-transfer reaction with polarization potential

In the case of $LiMn_2O_4$ cathode, the SEI layer plays an important role for lithium intercalation/deintercalation. A stable SEI can inhibit the further decomposition of electrolyte on the positive electrode and stabilize the positive electrode.

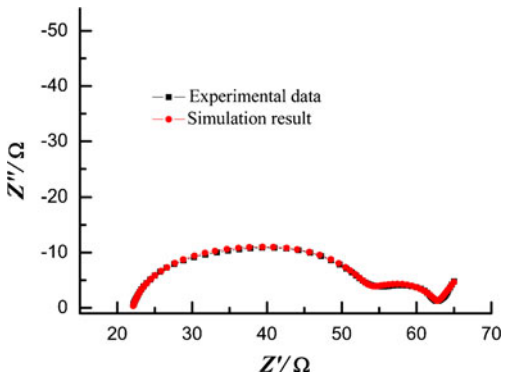

Fig. 9 Comparison of EIS experimental data at 3.95 V in the first charge process with simulation results using equivalent circuit of Fig. 7 for $LiMn_2O_4$ by hydrothermal route

Table 1 Equivalent circuit parameters obtained from Fig. 6 at 3.95 V for spinel $LiMn_2O_4$ prepared by hydrothermal route

Parameters	Valves	Uncertainty (%)
R_{SEI}	16.15	8.722
$Q_{SEI\text{-}Y0}$	0.000028908	5.6033
$Q_{SEI\text{-}n}$	0.87328	0.95976
R_e	15.45	10.063
$Q_{e\text{-}Y0}$	0.000086265	6.525
$Q_{e\text{-}n}$	0.92599	2.5958
R_{ct}	8.876	3.2221
$Q_{dl\text{-}Y0}$	0.0068639	3.7447
$Q_{dl\text{-}n}$	0.88256	2.0955
$Q_{D\text{-}Y0}$	1.149	6.3192
$Q_{D\text{-}n}$	0.68865	3.1297

Therefore, the life, charge–discharge, and safety performance of lithium-ion batteries are highly dependent on the SEI film of the electrode. Figure 10 shows variations of R_{SEI} with electrode potential obtained from fitting the experimental impedance spectra of spinel $LiMn_2O_4$ electrode prepared by hydrothermal and sol–gel methods individually during the first charge cycle. As can be seen, both R_{SEI} remain almost invariable with the increase of polarization potential in the first charge process, indicating that the SEI remains persistent and stable to a certain extent in those processes. However, the R_{SEI} of the $LiMn_2O_4$ by hydrothermal route slightly decreases at 4 V or more; this may be due to the dissolution of the resistive SEI film as proposed by Zhang et al. [36].

According to SEI model, the relation of R_{SEI} and resistivity ρ can be expressed as the below following:

$$R_{SEI} = \rho l/S \quad (4)$$

Where l is the thickness of SEI film, S is the surface area of electrode. If the values of resistivity ρ and electrode surface area S of the $LiMn_2O_4$ electrode are invariable or

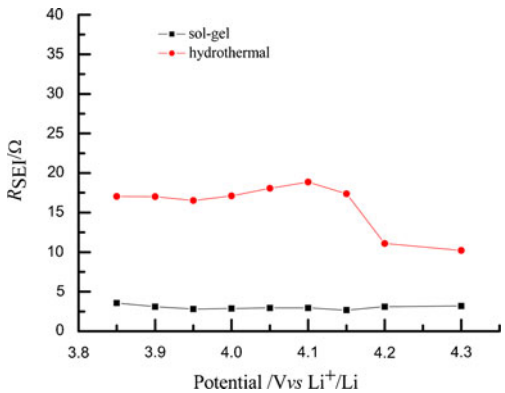

Fig. 10 Variations of R_{SEI} with electrode potential obtained from fitting the experimental impedance spectra of the spinel $LiMn_2O_4$ electrode during the first charge cycle

little variable, obviously a large impedance of R_{SEI} means a large SEI thickness. From Fig. 10, the R_{SEI} value of the $LiMn_2O_4$ prepared by hydrothermal route is larger than that of the $LiMn_2O_4$ synthesized by sol–gel method, that is, the SEI layer of the former is thicker than the one for the later. If the SEI layer on the cathode is not thick enough to prevent electron tunneling through it, an irreversible electrolyte reduction decomposition would further proceed. So the cycling performance of $LiMn_2O_4$ prepared by hydrothermal route with enough SEI layer thickness is better than the one by sol–gel with thin SEI layer.

Among the characteristics of insertion materials, the electrical conductivity is one of the most important issues in connection with the rate performance of batteries. In addition, conductivity measurements during the lithium insertion/extraction reaction would be an attractive approach to study the variation in the electronic structure of the materials as a function of lithium content [37, 38].

Variations of R_e with electrode potential obtained from fitting the experimental impedance spectra of spinel $LiMn_2O_4$ electrode during the first charge cycle are shown in Fig. 11. The electronic resistances of the electrode materials in the charge process have the same change tendency with potentials, namely, R_e first decrease and then increase with the increase of the electrode polarization potential in the charge process, in accordance with the experiment results obtained by Nishizawa et al. [39]. Spinel $Li_{1-x}Mn_2O_4$ is a mixed-valence (Mn^{3+}/Mn^{4+}) compound and its electronic conduction takes place by electron-hopping between high-valence (Mn^{4+}) and low-valence (Mn^{3+}) cations [40, 41].

Conductivity of this type would be governed by the amount of carrier of electron of Mn^{3+} and the hopping length of (Mn–Mn interatomic distance). The amount of electron carrier decreases proportionally with the degree of delithiation coupled with oxidation of Mn^{3+} to Mn^{4+}. On the other hand, the Mn–Mn distance in the spinel structure is contracted by delithiation. The R_e change may result from the sum of these opposite effects. The R_e decreases with the increase of the electrode polarization potential in the charge process, indicating that the effect of contraction of hopping length was more predominant than the decrease of the amount of the electron carrier.

Variations of charge-transfer resistance with polarization potential

Base on the Eqs. 1 and 2, the basic reaction mechanism of lithium-ion intercalation in $LiMn_2O_4$ cathode is illustrated as Eq. 5:

$$(1-x)Li^+ + (1-x)e^- + Li_xMn_2O_4 \rightleftarrows LiMn_2O_4 \quad (5)$$

Firstly, suppose that the velocity of the forward reaction r_f (intercalation of lithium ion in the $LiMn_2O_4$ electrode) is proportional to $c_T(1-x)$ and the concentration (M^+) of lithium ion in the electrolyte near the electrode. $c_T(1-x)$ represents the intercalation sites on the $LiMn_2O_4$ electrode surface unoccupied by lithium ions, wherein x is the intercalation level, c_T (mol/cm^3) is the maximum concentration of lithium ion in $LiMn_2O_4$ electrode. Then, deintercalation rate r_b is proportional to c_T x which represents occupied sites by lithium ion. So the intercalation velocity r_f and the deintercalation velocity r_b can be expressed as [42, 43]:

$$r_f = k_f c_T (1-x) M^+ \quad (6)$$

$$r_b = k_b c_T x \quad (7)$$

Therefore,

$$i = r_f - r_b = nFc_T((k_f(1-x)M^+ - k_b x) \quad (8)$$

Where n is the number of exchange electron on charging and discharging, F is the Faraday constant.

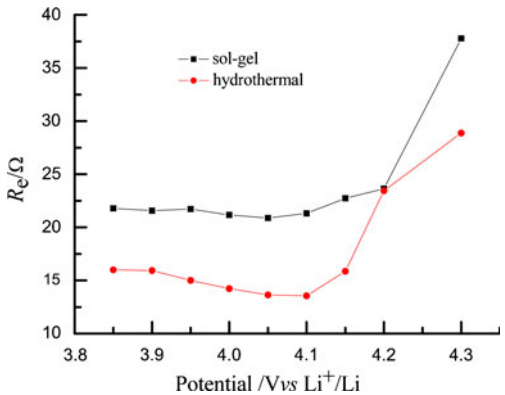

Fig. 11 Variations of R_e with electrode potential obtained from fitting the experimental impedance spectra of the spinel $LiMn_2O_4$ electrode during the first charge cycle

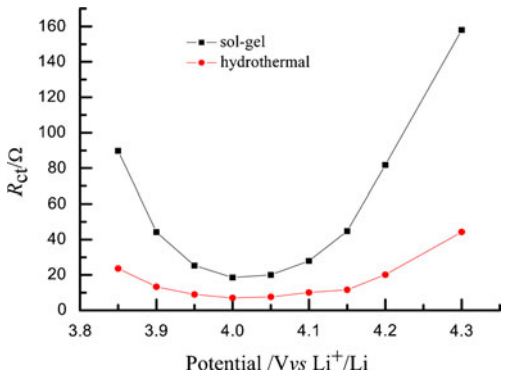

Fig. 12 Variations of R_{ct} with electrode potential obtained from fitting the experimental impedance spectra of the spinel $LiMn_2O_4$ electrode during the first charge cycle

The molar intercalation energy ΔG_{int} of lithium ion in the $LiMn_2O_4$ electrode can be expressed as:

$$\Delta G_{int} = a + gx \tag{9}$$

Where a is the constant about the interaction energy between an intercalated ion and a host lattice near it, and g is the constant about the interaction energy between two intercalated ions in different sites.

According to the activated complex theory, the relation of k_f and k_b with the potential as the below following:

$$k_f = k_f^0 \exp\left[\frac{-\alpha(nFe + \Delta G_{int})}{RT}\right] \tag{10}$$

$$k_b = k_b^0 \exp\left[\frac{1-\alpha(nFe + \Delta G_{int})}{RT}\right] \tag{11}$$

With α representing symmetry factor for the electrochemical reaction. The velocity constants k_f^0 and k_b^0can be expressed according to the Arrhenius form [40]:

$$k_f^0 = A_f \exp\left(\frac{-\Delta G_{0c}}{RT}\right) \tag{12}$$

$$k_b^0 = A_b \exp\left(\frac{-\Delta G_{0a}}{RT}\right) \tag{13}$$

Substitute Eqs. 10 and 11 into Eq. 8, the current i can be obtained in the following expression:

$$\begin{aligned} i = {} & nFc_T k_f^0 (1-x) M^+ \exp\left[\frac{-\alpha(nFe + \Delta G_{int})}{RT}\right] \\ & - nFc_T k_b^0 x \exp\left[\frac{(1-\alpha)(nFe + \Delta G_{int})}{RT}\right] \end{aligned} \tag{14}$$

On the equilibrium state, $E=E_e$, i =0. Therefore, exchange current density i_0 can be written as:

$$\begin{aligned} i_0 = {} & nFc_T k_f^0 (1-x) M^+ \exp\left[\frac{-\alpha(nFe + \Delta G_{int})}{RT}\right] \\ = {} & nFc_T k_b^0 x \exp\left[\frac{(1-\alpha)(nFe + \Delta G_{int})}{RT}\right] \end{aligned} \tag{15}$$

Thus,

$$i_0 = nFc_T k_0 (M^+)^{(1-\alpha)} (1-x)^{(1-\alpha)} x^{\alpha} \tag{16}$$

Where k_0 is the standard reaction speed constant and can be expressed as:

$$\begin{aligned} k_0 = {} & k_f^0 \exp\left[\frac{-\alpha(nFE_0 + \Delta G_{int})}{RT}\right] \\ = {} & k_b^0 \exp\left[\frac{(1-\alpha)(nFE_0 + \Delta G_{int})}{RT}\right] \end{aligned} \tag{17}$$

The charge-transfer resistance can be defined as:

$$R_{ct} = RT/nFi_0 \tag{18}$$

The substitution of expressions 14 and 16 into Eq. 18 gives the following formula:

$$R_{ct} = \frac{RT}{n^2F^2c_T k_0 (M^+)^{(1-\alpha)} (1-x)^{(1-\alpha)} x^{\alpha}} \tag{19}$$

If the reaction of lithium-ion intercalation and deintercalation in the $LiMn_2O_4$ electrode is invertible, α will be equal to 0.5.

Then,

$$R_{ct} = \frac{RT}{n^2F^2c_T k_0 (M^+)^{0.5} (1-x)^{0.5} x^{0.5}} \tag{20}$$

Equation 20 predicts clearly a rapid increase in R_{ct} with the decrease of x as $x<0.5$ and a rapid decrease in R_{ct} with the increase of x as $x>0.5$. The minimum R_{ct} can be attained when $x=0.5$. Equation 20 can well explain the relation between the charge-transfer resistance and electrode polarization potential which is illustrated in Fig. 12.

Conclusions

The spinel $LiMn_2O_4$ powders with submicro-size and excellent phase-pure particles were synthesized by hydrothermal route and sol–gel method. The $LiMn_2O_4$ powder prepared by hydrothermal route has good electrochemical properties of a specific capacity of 114.36 and 99.78 mAh g^{-1} at the 100th cycle; however, the one by sol–gel has only the capacity of 98.67 and 60.25 mAh g^{-1} at the 100th cycle, which means that even with the same chemical composition and crystal structure, the synthesis method and variation in physical properties of the cathode materials strongly influenced their electrochemical properties. The differently synthesized $LiMn_2O_4$ electrodes have the same change tendency of EIS. While the medium frequency arc to charge-transfer reaction of hydrothermally synthesized $LiMn_2O_4$ emerges in the potential region from 3.75 to 3.8 V and in the 3.85–3.9 V range for sol–gel prepared $LiMn_2O_4$. The selected equivalent circuit can fit well the EIS results of synthesized $LiMn_2O_4$.

Acknowledgments The project was supported by the National Key Basic Research Program of China (973) (2009CB220102), Fundamental Research Funds for the Central Universities (2010LKHX03, 2010QNB04, 2010QNB05) and Science and Technology "Climbing" Program of China University of Mining & Technology (ON090237).

References

1. Meqahed S, Scrosati B (1994) J Power Sources 51:79–104
2. Winter M, Brodd J (2004) Chem Rev 104:4250–4270
3. Yamada A, Miura K, Hinokuma K, Tanaka M (1995) J Electrochem Soc 142:2149–2156
4. Park HS, Hwang SJ, Choy JH (2001) J Phys Chem B 105:4860–4866
5. Kovacheva D, Gadjov H, Petrov K, Mandal S, Lazarraga MG, Pascual L, Amarilla JM, Rojas RM, Herrero P, Rojo JM (2002) J Mater Chem 12:1184–1188
6. Li GH, Ikuta H, Uchido T, Wakihara M (1996) J Electrochem Soc 143:178–182
7. Pistoia G, Antonini A, Rosati R, Bellitto C, Ingo GM (1997) Chem Mater 9:1443
8. Arora P, Popov BN, White RE (1998) J Electrochem Soc 145:807–814
9. Strobel P, Ibarra Palos A, Anne M, Le Cras F (2000) J Mater Chem 10:429–436
10. Thackeray MM, Johnson PJ, Picciotto LA, Bruce PG, Goodenough JB (1984) Mater Res Bull 19:179–187
11. Nagaura T, Yokokawa M, Hasimoto T (1989) US Patent 4:828
12. Kushida K, Kuriyama K (2000) Appl Phys Lett 76:2238–2240
13. Kang SH, Goodenough JB, Rabenberg LK (2001) Chem Mater 3:1758–1764
14. Choi S, Manthiram A (2000) J Electrochem Soc 147:1623–1629
15. Chuan Wu, Wang Zhao xiang, Feng Wu, Liquan Chen, Xuejie Huang (2001) Solid State Ion 144:277–285
16. Himmrich J, Lutz HD (1991) Solid State Commun 79:447–452
17. Chitra S, Kalyani P, Mohan T, Massot M, Ziolkiewicz S, Gangandharan R, Eddrief M, Julien C (1998) Ionics 4:8–16
18. Zhuang QC, Fan XY, Xu JM, Chen ZF, Dong QF, Jiang YX, Huang L, Sun SG (2006) Acta Phys Chim Sin 22:234–238
19. Lu DS, Li WS (2003) Acta Chimica Sinica 61:225–229
20. Goodenough JB, Thackeray MM, David WF, Bruce PG (1984) Revue de Chimie Minerale 21:435–455
21. Mosbah A, Verbaere A, Tournoux M (1983) Mater Res Bull 18:1375–1381
22. Pasquier AD, Blyr A, Courjal P, Larcher D, Amatucci G, Gerand B, Tarascon JM (1999) J Electrochem Soc 146:428–436
23. Cho J, Thackeray MM (1999) J Electrochem Soc 146:3577–3581
24. Jang DH, Shin YJ, OH SM (1996) J Electrochem Soc 143:2204–2211
25. Xia Y, Zhou Y, Yoshio M (1997) J Electrochem Soc 144:2593–2600
26. Robertason AD, Lu SH, Howard WF (1997) J Electrochem Soc 144:3505–3512
27. Xia Y, Yoshio M (1997) J Power Sources 66:129–133
28. Aurbach D, Markovsky B, Shechter A (1996) J Electrochem Soc 143:3809–3820
29. Vincent CA (2000) Solid State Ion 134:159–167
30. Gao Y, Dahn JR (1996) Solid State Ion 84:33–40
31. Barboux P, Tarascon JM, Shokoohi FK (1991) J Solid State Chem 94:185–196
32. Tarascon JM, Mckinnon WR, Coowar F, Bowmer TN, Amatucci G, Guyomard D (1994) J Electrochem Soc 141:1421–1431
33. Zhuang QC, Tao W, Du LL, Cui YL, Fang L, Sun Z (2010) J Phys Chem C 114:8614–8621
34. Gnanaraj JS, Cohen YS, Levi MD, Aurbach D (2001) J Electroanalyt Chem 516:89–102
35. Aurbach D, Markovsky B, Levi MD, Levi E, Schechter A, Moshkovich M, Cohen Y (1999) J Power Sources 81–82:95–111
36. Zhang SS, Xu K, Jow TR (2002) J Electrochem Soc 149:A586–A590
37. Molenda J (2004) Solid State Ion 175:203–213
38. Molenda J (2005) Solid State Ion 176:1687–1694
39. Nishizawa M, Ise T, Koshika H, Itoh T, Uchida I (2000) Chem Mater 12:1367–1372
40. Pistoia G, Zane D, Zhang Y (1995) J Electrochem Soc 142:2551–2557
41. Marzec J, Świerczek K, Przewoźnik J, Molenda J, Simon DR, Kelder EM, Schoonman J (2002) Solid State Ion 146:225–237
42. Barrel G, Diard JP, Montella C (1984) Electrochim Acta 29:239–246
43. Li Y, Wu H (1989) Electrochim Acta 34:157–159